García Castillo, F.; Cortés Pérez, J.; Amigó Borrás, V.; Sánchez Arévalo, P.; Lara Rodríguez, G. (2015). Development of a stress-induced martensitic transformation criterion for a Cu-Al-Be polycrystalline shape memory alloy undergoing uniaxial tension. Acta Materialia. 97:131-145. doi:10.1016/j.actamat.2015.06.044.

Development of a stress-induced martensitic transformation criterion for a Cu-Al-Be polycrystalline shape memory alloy undergoing uniaxial tension

F. N. García-Castillo,[a,*], J. Cortés-Pérez[b], V. Amigó[c], F. M. Sánchez-Arévalo[d], G. A. Lara-Rodríguez[d]

[a] Posgrado de Ingeniería, Facultad de Ingeniería, Universidad Nacional Autónoma de México, Circuito Exterior, Ciudad Universitaria, México, D.F. C.P. 04510.

fer_nes@hotmail.com*

[b] Centro Tecnológico Aragón, FES Aragón, UNAM. Av. Rancho Seco s/n, Col. Impulsora, Cd. Nezahualcóyotl, Estado de México, México, C.P. 57130.

jacop@unam.mx.

[c] Universitat Politècnica de València, Instituto de Tecnología de Materiales, Camino de Vera s/n, C.P. 46022.

vamigo@mcm.upv.es.

[d] Instituto de Investigaciones en Materiales, Universidad Nacional Autónoma de México Apdo. Postal 70-360, Cd. Universitaria, México, D. F. C.P. 04510.

fsanchez@iim.unam.mx, laragab@iim.unam.mx

* Corresponding Author.

Phone: (01 55) 56 23 09 70

E-mail address: fer_nes@hotmail.com

ABSTRACT

This study presents a criterion for predicting the martensitic variants (*MVs*) that appear during the stress-induced martensitic transformation (*SIMT*) in a polycrystalline sample of Cu-11.5% wt. Al-0.5% wt. Be under simple tension. Our criterion is based on crystallographic parameters, such as the crystal orientation and Schmid factor (*SF*). The displacement vector fields (*DVFs*) were obtained in the observation system by a mathematical model and were used to distort the boundary of a set of grains. From the *DVF*, the strain tensor for each grain was obtained, and the strain ratio (*SR*) in the observation system was calculated. Electron backscattering diffraction (*EBSD*) measurements were performed to determine the crystal orientation of the grains. The inverse *SF* was used to determine the in-plane stress transformation diagrams (*STDs*) for each studied grain. The combination of a balance criterion (*BC*) and *STD* provided a criterion that allowed us to predict the possible order of stress-induced *MVs* formed as a function of the crystal orientation and thermomechanical parameters of the shape memory alloy (*SMA*) with higher accuracy than when using the criteria separately. To validate our criteria, we tested other researchers' published results. Our results were in agreement and were capable of predicting the stress-induced *MVs* in a polycrystalline *SMA*.

Keywords: Shape memory materials, Grain interaction, Stress-induced martensitic transformation, *EBSD*.

1. Introduction

In mechanical engineering applications, shape memory alloys (*SMAs*) are considered interesting materials due to their well-known effects. Such applications are focused on the development of sensor/actuator devices, which were recently applied to energy recovery [1-6]. Some of these applications would be quite complicated if conventional materials were used. The creation of new devices with *SMAs* requires the use of mathematical models that consider the associated effects of these materials and mimic their mechanical behavior appropriately.

Research conducted on these alloys indicates that their mechanical behavior is complex because of their highly anisotropic nature, non-linear mechanical behavior, hysteresis, and temperature dependence [7-11]. For these reasons, previous studies have focused on single crystals [12-17]. However, the vast majority of applications require polycrystalline materials; therefore, some research has been conducted to understand the mechanical behavior of *SMA* polycrystals, and mathematical models and experimental results have been reported [18-20]. In fact, the relation between microstructure and macromechanical behavior has posed an interesting research problem for many years. The mechanical behavior of *SMAs* composed of polycrystalline materials is strongly altered by effects associated with their microstructure. For this reason, studies related to the stress-induced martensitic transformation (*SIMT*) of polycrystalline *SMAs* have taken into account specific issues such as the Hall-Petch relationship, grain interaction (*GI*) and the Schmid factor (*SF*) [21-28]. For example, according to Montecinos et al. [21], the change in the mechanical behavior of Cu-Al-Be under stress depends on its grain size. These results indicate a Hall-Petch-type relationship; however, the authors did not consider the crystallographic

orientation and the martensitic variants (*MVs*) formed in each grain. Berveiller et al. [22] performed an in situ study of the lattice rotation of an individual grain during the *SIMT* of Cu-Al-Be samples subjected to a tensile load at room temperature. These authors observed small changes in the crystal orientation after the inverse *SIMT*. Siredey et al. [23] developed a thermomechanical model that considers the interaction between the *MVs* of a grain and obtained an equation to mimic the interaction energy for more than two Cu-Al-Be *MVs*. Sánchez-Arévalo et al. [24] used a digital image correlation technique to obtain the displacement vector fields (*DVFs*) in a Cu–Al 11.2 wt.%–Be 0.6 wt.% *SMA* during the *SIMT* in a simple tensile test. Martínez-Fuentes et al. [25] applied the methodology developed by Sánchez-Arévalo et al. to observe the micromechanical and macromechanical behavior of a Cu-Al 11.2 wt.%-Be 0.6 wt.% polycrystal and a Cu-Al 11.2 wt.%-Be 0.5 wt.% single crystal *SMA* undergoing a *SIMT* induced by 3-point bending. These authors observed *GI* in the 2D confined grains, possibly because the interaction between the growing *MV* modified the local state of stress in the grain and neighboring grains. The martensitic phase re-orients with increasing load, which provokes the growth of several *MVs* in different directions; this finding was in good agreement with the stress transformation diagrams (*STDs*) for Cu-Al-Be alloys. However, this study did not consider the crystallographic aspect of each grain studied.

The *SIMT* in *SMAs* provides a good opportunity to compare plasticity criteria to obtain other essential aspects of *SMAs*, such as the *SF*. Recently, some researchers have used the *SF* to study the *SIMT* in polycrystalline samples [26-28]. For example, Kaouache et al. [27] used this factor to verify the formation of *MVs* in polycrystalline samples during the *SIMT*, expanding the application of the *SF* criterion, which is typically used in single crystals, to polycrystalline samples.

In addition, mathematical models have been developed to mimic the macromechanical and micromechanical behavior of *SMAs*; specifically, we focus on the model of Cortés-Pérez [29]. This model is used to simulate the distortion of the sample surface and obtain the strain and displacement fields of an *SMA* undergoing the *SIMT* as a function of the crystalline orientation. The Cortés-Pérez model [29] consists of a mathematical description of the *DVF* present in a sample during the *SIMT*. This *DVF* is non-homogeneous and is defined in a reference system matching the transformation system (X_T, Y_T, Z_T), where the unit base in the system is $(e_{T_1}, e_{T_2}, e_{T_3})$, as shown in Figure 1. The other two systems used in this research appear in this figure as (X, Y, Z) and (X_0, Y_0, Z_0) with unit bases (e_1, e_2, e_3) and (e_{01}, e_{02}, e_{03}), respectively.

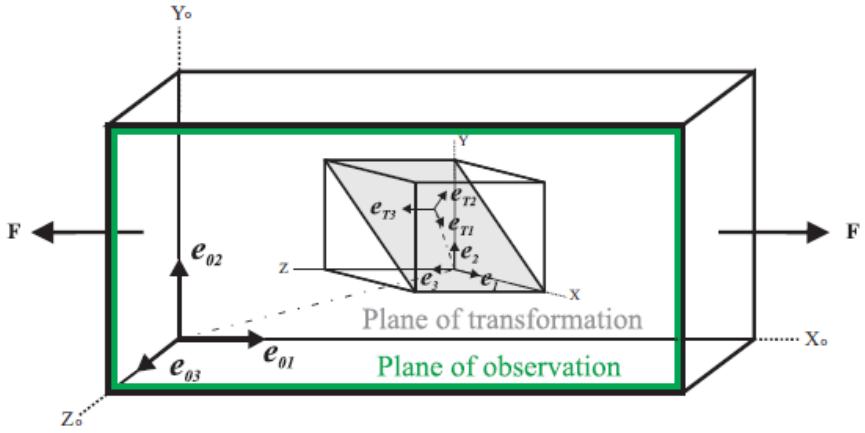

Figure 1. Vector space basis used in the Cortes-Pérez model [29]: Transformation basis e_{Ti}, Observation basis e_{Oi}, and "Canonic" basis e_i, i = 1, 2, 3.

The *DVF* $u(x_T, y_T, z_T)$ is defined for each transformation element (24 *MVs*); this vector field can be expressed by a habit plane $(n_1 \quad n_2 \quad n_3)$ and a shear direction $[m_1 \quad m_2 \quad m_3]$ with coordinates (x_T, y_T, z_T). This *DVF* can be written as follows:

$$u(x_T, y_T, z_T) = \begin{pmatrix} \delta f h w(y_T) \\ 0 \\ 0 \end{pmatrix} \tag{1a}$$

$$w(y_T) = \begin{cases} 0; -\infty \le y_T \le 0 \\ \frac{y_T}{hf}; 0 \le y_T \le hf \\ 1; hf \le y_T \le h \end{cases} \quad (1b)$$

where δ is the shear amplitude value and h is the length of the martensitic plate along the y_T direction.

Thus, $w(y_T)$ is re-defined using a smoothing double hyperbole:

$$w(y_T) = \frac{fh + \sqrt{{r_0}^2 + {y_T}^2} - \sqrt{{r_0}^2 + (y_T - fh)^2}}{2fh} \quad (2)$$

where r_0 is the radius of the transition of the martensitic-austenite boundaries and f is the volumetric fraction, a scalar value depending on the applied stress, test-temperature, and *SMA* parameters. The volumetric fraction is defined by Equation 3,

$$f = \frac{e^{\frac{\ln(9)(2\sigma - \sigma_c - \sigma_f)}{\sigma_f - \sigma_c}}}{1 + e^{\frac{\ln(9)(2\sigma - \sigma_c - \sigma_f)}{\sigma_f - \sigma_c}}} \quad (3)$$

where σ is the applied effective stress (for the simple tension test, the applied effective stress is defined by the ratio of shear stress/*SF*, τ/m). σ_c and σ_f are the effective critical stresses at the beginning and end of the *SIMT*, respectively, at test temperature *T*; these stresses can be calculated by the following equations, which consider the Clausius-Clapeyron ratio:

$$\sigma_c = \frac{\partial \sigma_c}{\partial M_s}(T - M_s) \quad (4)$$

$$\sigma_f = \frac{\partial \sigma_c}{\partial M_s}\left(T - M_f\right) \quad (5)$$

where M_S and M_f are the critical temperatures at the beginning and end of the martensitic transformation, respectively, which depend on the chemical composition and grain size, among other factors. The *DVF* is defined in the observation system and denoted as

$$(x_T, y_T, z_T)^T = A_{X_0 \to X_T}(x_0, y_0, z_0)^T \quad (6)$$

$$u(x_0, y_0, z_0) = A_{X_T \to X_0} u(x_T, y_T, z_T) = A_{X_T \to X_0}\, u\left(\left(A_{X_0 \to X_T}(x_0, y_0, z_0)^T\right)^T\right) \quad (7)$$

where the relation of the three-vector space basis used in this research is

$$A_{X_T \to X_0} = A_{X \to X_0} A_{X_T \to X} \quad (8)$$

The $A_{X_T \to X_0}$ matrix is used to change the basis from the transformation to observation system as a function of grain orientation and is defined as

$$A_{X \to X_T} = \left[A_{X_T \to X}\right]^{-1} = \sum_{i=1}^{3} \{e_i\}_{X_T} \otimes e_i \quad (9)$$

$$A_{X_T \to X} = \sum_{i=1}^{3} \left\{e_{T_i}\right\}_X \otimes e_{T_i} = \begin{pmatrix} m_1 & p_1 & n_1 \\ m_2 & p_2 & n_2 \\ m_3 & p_3 & n_3 \end{pmatrix} \quad (10)$$

$$A_{X \to X_0} = \left[A_{X_0 \to X}\right]^{-1} = \sum_{i=1}^{3} \{e_i\}_{X_0} \otimes e_i \quad (11)$$

$$A_{X_0 \to X} = \sum_{i=1}^{3} \{e_{0i}\}_X \otimes e_{0i} = \begin{pmatrix} u & c_1 & h \\ v & c_2 & k \\ w & c_3 & l \end{pmatrix} \quad (12)$$

where $[h\ k\ l]$ is the sample normal (*SN*) and $[u\ v\ w]$ is the rolling direction (*RD*); the coordinates of the *RD*, (x_0, y_0, z_0), are obtained from electron backscattering diffraction (*EBSD*); $(n_1\ n_2\ n_3)$ is the habit plane; and $[m_1 m_2 m_3]$ is the direction of the strain shear. Its coordinates are (x_T, y_T, z_T). Both of these arrays are described by the canonic vector space basis, which is defined by the unit cell of the austenite phase. These transformation systems are different for each *SMA*. In addition, the transversal direction (*TD*) can be determined by the cross product of the *SN* and *RD*. Similarly, the third direction in the transformation system is determined by the cross product of the habit plane and the direction of deformation in each base:

$$\begin{pmatrix} p_1 \\ p_2 \\ p_3 \end{pmatrix} = \begin{pmatrix} m_1 \\ m_2 \\ m_3 \end{pmatrix} \times \begin{pmatrix} n_1 \\ n_2 \\ n_3 \end{pmatrix} \quad (13)$$

$$\begin{pmatrix} c_1 \\ c_2 \\ c_3 \end{pmatrix} = \begin{pmatrix} u \\ v \\ w \end{pmatrix} \times \begin{pmatrix} h \\ k \\ l \end{pmatrix} \quad (14)$$

Finally, the strain tensor is defined as the symmetric part of the displacement field gradient:

$$\varepsilon_{Tr} = \frac{1}{2}\left[grad\left(u(x_0, y_0, z_0)\right) + grad^T\left(u(x_0, y_0, z_0)\right)\right] \quad (15)$$

The literature contains detailed accounts of extensive efforts to understand the nature of the *SIMT*; some of which have considered the crystal orientation and *SMA* parameters [27, 28]. However, research on the *SIMT* has yet to enable a prediction of the possible order of *MV* formation as a function of crystallographic and *SMA* parameters; therefore, the aim of our study is to develop a novel criterion that theoretically predicts the formation of *MVs* on the observation surface for a set of grains by considering the crystal orientation and the parameters of the *SMA*, including the critical temperatures, the Clausius-Clapeyron relationship, and the transformation system.

Our research considers 10 grains of two different polycrystalline samples of a Cu-11.5 wt. % Al-0.5 wt. % Be *SMA*. The first sample was elaborated in this research, and the second involves a sample tested by Kaouache et al. [27]; their results are considered in our study. The crystallographic orientation of each grain in our sample was measured using the *EBSD* technique. Hence, the 24 *MVs* were depicted in the observation system for all the studied grains and were compared with the *MVs* obtained during the *SIMT*. The strain ratio (*SR*) criterion was used to predict the *MVs*. The strain tensor was determined using the *DVF* obtained from the Cortés-Pérez model [29]. The *DVF* in the system of observation was used to distort the grain perimeter (obtained by digital image analysis of each studied

grain). Next, a set of three grains with a common triple point was compared before and after the transformation. Because the |*SR*| and *SF* criteria were not sufficient to allow a prediction of the *MVs*, an additional criterion was introduced, which considers the balance between both the |*SR*| and the *SF* criteria to predict the order of formation of the *MVs*. This criterion is complemented with the in-plane *STDs.*

2. Experimental details

A polycrystalline sample of Cu-11.5% wt. Al-0.5% wt. Be was produced by conventional casting techniques in a high-frequency furnace. This alloy was elaborated using Belkahla's equation [30]. An ingot was obtained from this cast. Then, thin slides were cut to 18 × 10 × 1.2 mm (l × w × t) using an Accuttom-5 automatic precision cut-off machine from Struers Izasa S.A. (Barcelona, Spain). A recirculation-cooling unit with a flow rate of 800 ml/min and a constant speed of 0.025 mm/s was used.

From the thin slides, one sample was obtained with a reduced-center section of 4 mm. After sample preparation, the samples were betatized (750°C for 15 min and 100°C for 20 min) according to the method of Flores [31]. Then, the M_S temperature was determined using a TA Instruments Q100 differential scanning calorimeter (*DSC*) (New Castle, Delaware, United States) with a 39.45 mg sample. *DSC* was performed over a temperature range from –80 to 200°C at a rate of 20°C/min.

To observe the crystalline microstructure of these materials, the tensile samples were prepared for metallography according to the standards of Struers for Cu preparation; because of the size of the samples, only mechanical polishing was used under small applied loads, avoiding the *SIMT*. This metallographic preparation was adequate for *EBSD*

measurements, which were performed to detect the crystalline orientation of the grains. The *EBSD* measurements were performed in a *JEOL* model *JSM 6300* scanning electron microscope with *INCA* software. In this software, the crystallographic parameters of Cu-Al-Be must be input as follows: DO_3 *BCC*, a_o = *5.82* Å and special group $Fm\bar{3}m$ *(225)* [32]. The uniaxial tensile tests were then conducted on a Deben-Gatan Microtest tensile device (Gatan, Inc., Pleasanton, California, United States), which was coupled to an optical microscope from Leica MZ APO. The equipment included a 2 kN load cell, and the deformation rate of these tests was 0.2 mm/min. The *SIMT* was also observed in situ. A specially programmed virtual instrument in LabView was used to detect grain boundaries, registering a set of (*x, y*) points, which defined the geometry of each grain. This analysis was conducted after the *EBSD* measurements because *EBSD* was able to reveal the grains without any chemical etching. A front panel of the grain-boundary detection virtual instrument is presented in Figure 2.

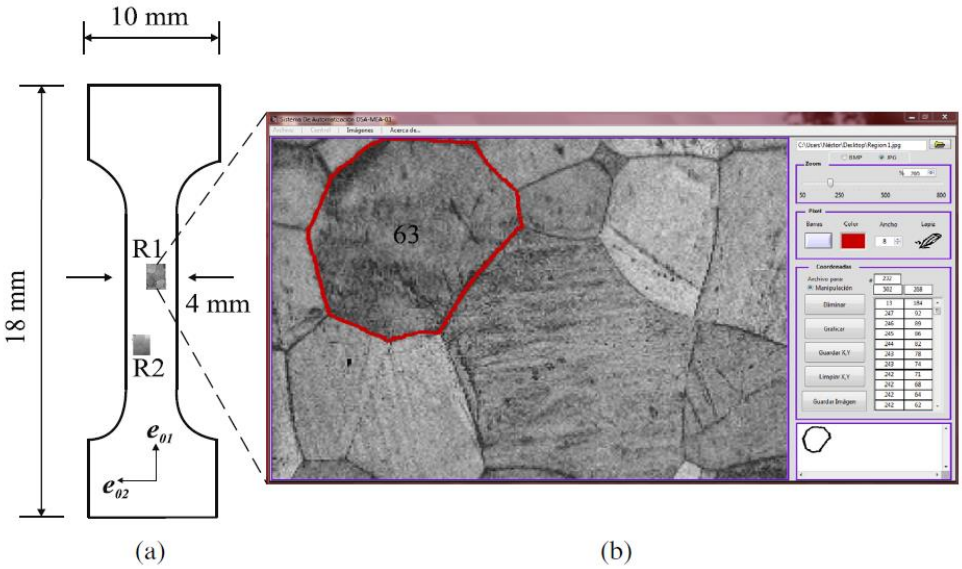

Figure 2. Digital images used for the detection of a grain perimeter. a) Tensile sample illustrating the dimensions and specific studied regions. b) Front panel of the virtual instrument, which shows the window corresponding to the "routine" to select and record points on the boundaries of the grain.

The parameters used for the *Cu-Al-Be* sample in our calculations were M_s = -20°C, based on *DSC* measurements; a Clausius-Clapeyron relation of $d\sigma/dT = 1.97\frac{MPa}{^\circ C}$ [33]; a shear amplitude of 0.2324; and the transformation system reported by Kajiwara et al. [34] for the Cu-Al system n = [0.17, 0.66, 0.72] and m = [0.16,−0.74, 0.64].

3. Results and discussion

Two separate regions were observed in our sample and are presented as regions *R1* and *R2* in Figure 2a. Only 3 grains were analyzed in each region. The crystalline orientation of grains is required to apply our *SIMT* criterion. Figures 3a and 3b present images of the microstructures in the austenite phase for regions *R1* and *R2* obtained from *EBSD* measurements; these figures provide the labels for the six grains analyzed in this study. The images are colored according to the crystal orientation depicted by the inverse pole figure, and the color key is provided in Figure 3c; Figures 3a and 3b were plotted on the *RD*. The *EBSD* measurements were obtained after the first cycle of uniaxial tension. The crystallographic details of these grains are summarized in Table 1.

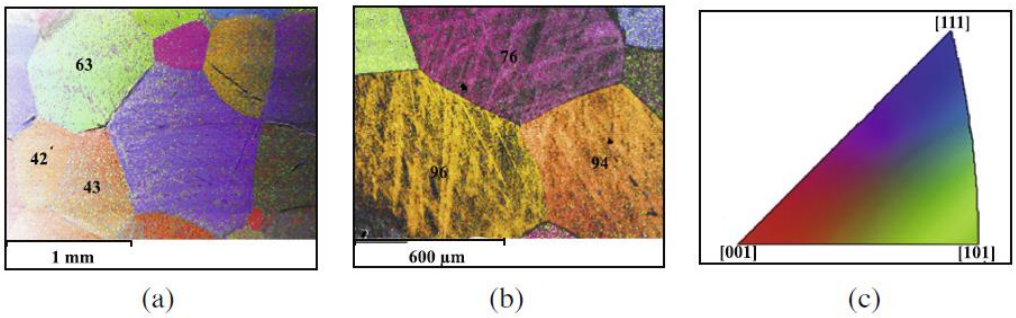

Figure 3. Measurements of the EBSD for the Cu-Al-Be *SMA*. a) Region 1 involving grains 42, 43, and 63. b) Region 2 involving grains 76, 94, and 96. c) Color key of the inverse pole figure.

Table 1. Crystallographic orientations of each grain studied in our sample.

Region 1			**Region 2**		
Grain	*RD*	*SN*	Grain	*RD*	*SN*
42	[0.19, 0.89, -0.39]	(0.10, -0.42, -0.89)	76	[-0.46, -0.85, -0.23]	(0.88, -0.41, -0.23)
43	[-0.42, 0.38, 0.81]	(0.10, 0.91, -0.37)	94	[0.88, -0.22, -0.41]	(0.40, -0.10, 0.90)
63	[0.15, 0.97, -0.15]	(0.78, -0.21,-0.57)	96	[0.86, 0.37, -0.34]	(0.39, -0.91, 0)

Figure 4 presents typical *MVs* formed by the *SIMT* of the studied grains; these plates are similar to those previously reported by other authors [23-28]. In this figure, our sample was at a specific stress higher than the critical stress of transformation, σ_c.

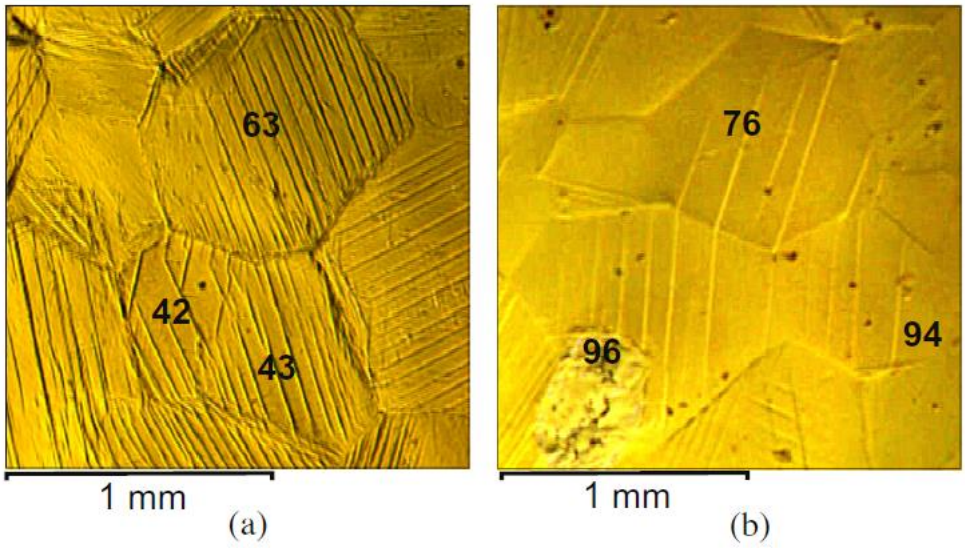

Figure 4. Formed *MVs* of each grain studied in our sample. a) Region 1. b) Region 2.

The grains contained in *R1* (42, 43 and 63) indicate that the vast majority of the *MVs* had a similar angle on the e_{01} axis; however, this result does not imply that the same stress-induced *MV* has been obtained. To prove this case, the crystallographic orientation of each grain and the transformation system reported by Kajiwara et al. [34] were used to obtain the 24 *MVs* for the observation system. The order of the transformation system in this research is the same as that reported by Kaouache et al. [27]. Each mark on the observation surface was calculated using the matrix for the change of basis applied to the corresponding habit

plane; their intersection with the observational plane was subsequently obtained. This analysis was performed for the six grains studied in our sample; however, Figure 5 only provides the diagram for grain 43.

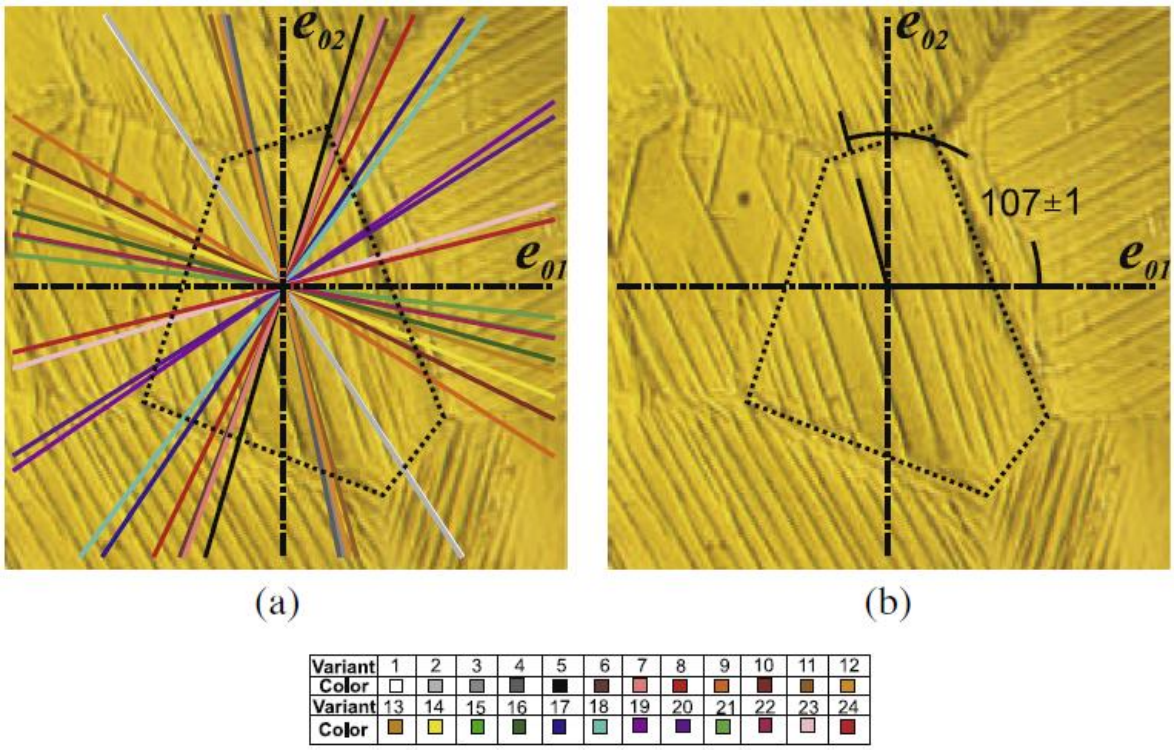

Figure 5. *MVs* formed and calculated in grain 43. a) Diagram of the 24 possible *MVs* overlapped on the metallographic image. b) Average angle formed between the e_{01} axis and the real *MV*.

The perimeter of grain 43 is denoted by a black dotted line, whereas the e_{01} and e_{02} axes (the *RD* and *TD* directions, respectively) are denoted by black dot-dashed lines, according to the basis defined in Figure 1. In relation to the color code of Figure 5, the important obtained *MVs* are 3, 4, 11, and 12 (gray, dark gray, light brown and light orange, respectively). The calculations show that four *MVs* calculated are coincident, with only one *MV* formed at $107 \pm 1°$ with respect to the e_{01} axis, as shown in Figure 5b. Similarly, the intersection of each habit plane with the observational plane was calculated for each grain, and the results are summarized in Table 2.

Table 2. Summary of the comparison between the formed and calculated *MVs* in our sample.

Region	Grain	*MVs* formed by grain	Calculated *MVs*	Angle deviation between calculated and formed MVs (°)
1	42	I	2	2.9°
		II	3	6.1°
			4	6.4°
			9	5.8°
			10	8.9°
	43	I	3	1.4°
			4	1.9°
			11	2.8°
			12	0°
	63	I	23	0°
			24	2.4°
		II	9	3.9°
			10	0°
			11	8°
			18	9.5°
			19	0.9°
			20	5.7°
		III	8	1.1°
			17	6.6°
2	76	I	17	2.5°
			18	6.5°
			23	1.1°
			24	1.9°
	94	I	5	3.7°
			6	4.8°
			15	6.2°
			16	3.8°
	96	I	17	2°
			18	0.5°

In addition, the *MVs* coincident with the real *MVs* were filed according to the number of *MVs* formed in each grain. For example, 3 *MVs* were formed in grain 63; therefore, calculated *MVs* 23 and 24 are coincident with only one of the formed *MVs*. Finally, Table 2 provides the angle deviation between the calculated and real *MVs* formed for each case. The selected *MVs* were within an angle of less than 10°, which suggests misalignment in the studied samples.

Because several *MVs* may match the real *MVs* for the grains, it was necessary to establish a criterion to select the real *MV* that grows in the plane of observation.

One method of discarding some *MVs* is the *SF* criterion, as previously reported by Kaouache et al. [27]. Table 3 presents three expected *MVs* with the highest *SF* for each grain, and the last column provides the *MVs* that matched those in Table 2 for the six studied grains in regions *R1* and *R2*.

Table 3. Expected and coincident *MVs*, according to the *SF* criterion, of grains studied in *R1* and *R2*.

Region	Grain	Expected *MVs*	Highest *SF*	Formed *MVs*
1	42	19	0.47	None
		24	0.42	None
		2	0.38	I
	43	11	0.36	I
		14	0.34	None
		3	0.29	I
	63	19	0.49	II
		2	0.49	None
		24	0.45	I
2	76	12	0.44	None
		2	0.39	None
		17	0.33	I
	94	23	0.45	None
		18	0.41	None
		15	0.37	I
	96	13	0.41	None
		18	0.39	I
		8	0.33	None

Our experimental results and the *SF* criterion indicated that only grains 43 and 63 satisfied the condition of the maximum *SF* criterion. These results are inconsistent with the criteria reported by Kaouache et al. [27]. For this reason, we performed an analysis to compare our results with those reported by Kaouache et al. [27]. This analysis was the same as that used for our samples. The 24 *MVs* in the observation system were calculated for all grains

reported by Kaouache et al. [27]. The real *MVs* formed and the calculated *MVs* are compared in Table 4. The *SF* for the 24 *MVs* of each grain reported by Kaouache et al. [27] was recalculated. We used the following crystallographic orientations to obtain the same *MVs* reported by Kaouache et al. [27] for grain *C—SN* (-0.84, -0.13, -0.52) and *RD* [0.27, −0.94, −0.16]—according to the method of Cortes et al. [35].

A comparison of the results from Tables 4 and 5 indicates that the *MV* with maximum *SF* is always present in the actual case, as described by Kaouache et al. [27]; nevertheless, the second *MV,* with a higher probability of growth, does not always satisfy this condition.

As previously discussed, our results indicate that the *MV* with the higher *SF* did not always grow. The third *MV* with a high *SF* (but not the highest) appeared in the plane of observation, as shown in Table 3 for grains 42, 43, 63, 76 and 94.

To explain why the third *MV* with a high *SF* value grows instead of the *MV* with maximum *SF*, we first calculated the strain tensor in the observation system and the *SR* $\left(\varepsilon_{xo}/\varepsilon_{yo}\right)$ for the three expected *MVs* with high *SFs* using the model of Cortés-Pérez [29]. Figure 6 illustrates the meaning of the *SR*. Specifically, this figure presents two patterns of distortion for grains from region 2. Both patterns of displacement were obtained in the mathematical model developed by Cortés-Pérez [29]. This model is able to simulate the displacement and deformation fields encountered by a grain during the growth of an *MV*.

Table 4. Summary of the comparison between the formed and calculated *MVs* for samples *P1* and *P2* reported by Kaouache et al. [27].

Sample	Grain	*MVs* formed by grain	Calculated *MVs*	Angle deviation between calculated and formed MVs (°)
P1	A1	I	3	0°
			4	0°
			11	7.2°
			12	7.4°
	B1	I	5	5.4°
			6	0°
			7	9.3°
			8	2°
		II	9	1.4°
			10	4.9°
			13	7.3°
			15	3.7°
			16	0.7°
		III	12	3.5°
			14	2.7°
			21	7.1°
			22	1.2°
	C1	I	9	5.4°
			10	1°
			15	1.8°
			24	6.5°
		II	19	0°
			20	0°
		III	21	4.9°
			22	0°
P2	A2	I	17	2.3°
			18	0°
		II	4	1.1°
			5	0.9°
			23	2.3°
			6	4.7°
		III	3	5.8°
			7	7.6°
			8	3.9°
			24	3.9°

Table 5. Expected and coincident variants, according to the *SF* criterion, of grains reported by Kaouache et al. [27]

Sample	Grain	Expected *MVs*	Highest *SF*	Formed *MVs*
P1	A1	4	0.42	I
		10	0.38	None
		6	0.26	None
	B1	6	0.47	I
		15	0.47	II
		21	0.32	III
	C1	10	0.49	I
		4	0.45	None
		22	0.45	III
P2	A2	18	0.40	I
		23	0.39	II
		3	0.33	III

Figure 6a presents the initial configuration of the perimeters of grains 76, 94, and 96 (without deformation and before the martensitic transformation). Then, applying the model of Cortés-Pérez [29] for each individual grain, a deformed configuration is obtained and shown in Figures 6b and 6c. This model also provides us with the *DVF* for each *MV* in each grain for two cases. The first case corresponds to the *DVF* associated with *MVs* that presented a maximum *SF* (*VMSF*), in which case the *DVF* presents a large displacement component in the *TD* (e_{02}). The second case corresponds to the *DVF* associated with *MVs* that presented a higher *SR* (*VHSR*), in which case the *DVFs* were largely aligned with the e_{01} direction. Considering both types of distortion (*VMSF* and *VHSR*), a *GI* effect was clearly observed. The *VMSF* distortion demonstrated a tensile state of stress, causing a grain separation trend, whereas the *VHSR* exhibited the opposite trend, with lower-magnitude compression and tension states of stress relative to those observed for *VMSF*. Both types of distortion can contribute strongly to the stress in these grains. This contribution might alter the growth of the expected *MVs* or even inhibit the growth of an *MV* with a maximum *SF*; this latter condition is stronger for *VHSR* distortion. Importantly,

strain compatibility is more likely to be preserved in *VHSR* than in *VMSF*. This tendency can be predicted by analyzing the strain tensor, namely, the proposed *SR*. Such an effect could be explained as a tendency for the material to employ the minimal mechanical energy, released during the tension test, to begin martensitic nucleation caused induced by stress. Finally, Figure 6d presents the actual stress-induced *MVs* for grains 76, 94, and 96. The *VHSR* clearly corresponds well with the actual *MVs* presented in Figure 6d.

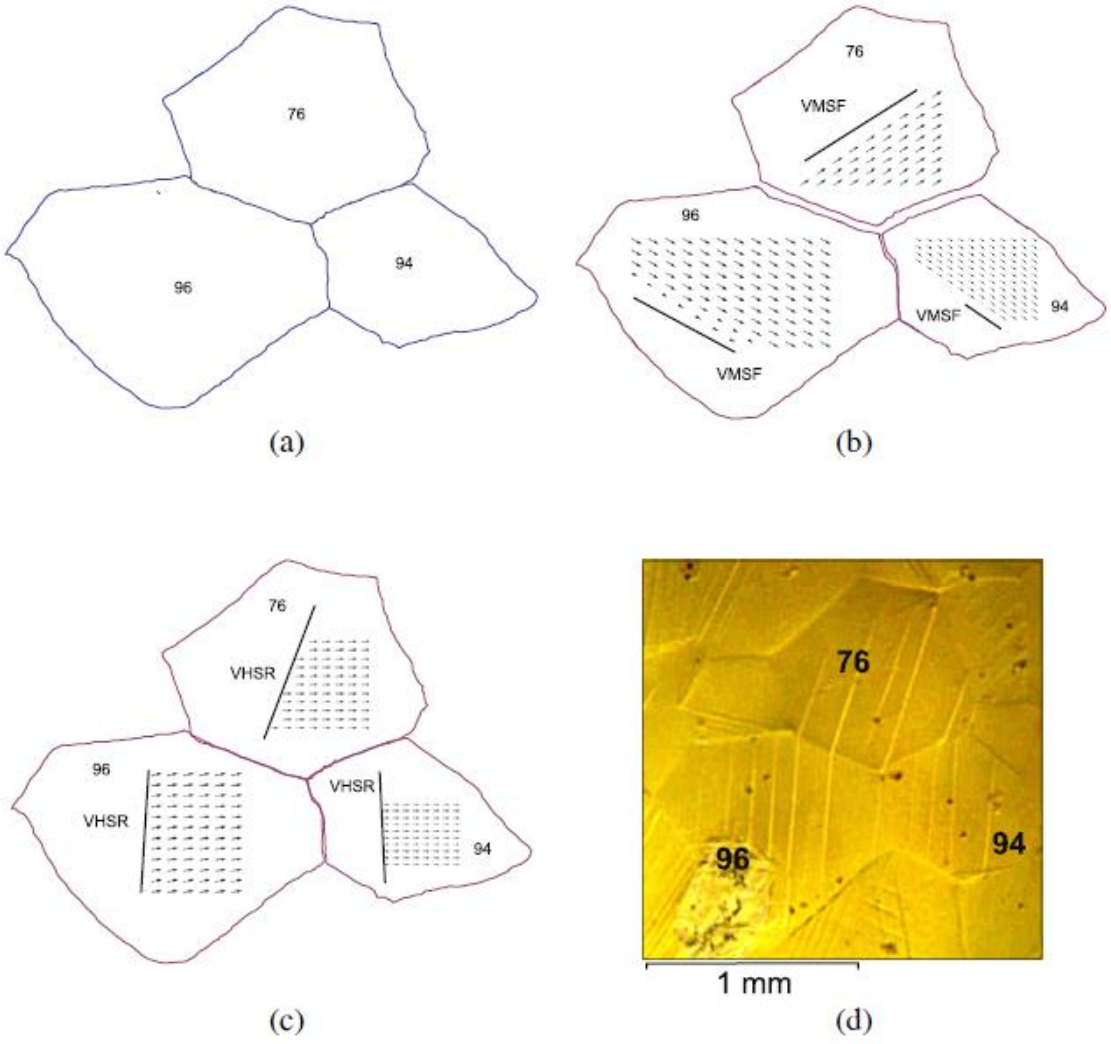

Figure 6. Comparison between the two grain boundaries under the *SIMT* for region 2. a) Original configuration. b) Distortion using the *MV* with maximum *SF* (*VMSF*), and c) distortion using the *MV* formed with higher *SR* $\left(\varepsilon_{xo}/\varepsilon_{yo}\right)$ (*VHSR*). d) Real *MVs* formed in each grain.

Figure 6 presents the analysis for three grains, although several additional grains were analyzed. The results of this analysis are summarized in Table 6.

Table 6. Strain tensor analysis for our grains according to the |*SR*| criterion using the model of Cortés-Pérez [29].

Region	Grain	Expected *MVs*	Strain tensor $\begin{pmatrix} \boldsymbol{\varepsilon_{xo}} & \boldsymbol{\gamma_{xyo}} \\ \boldsymbol{\gamma_{xyo}} & \boldsymbol{\varepsilon_{yo}} \end{pmatrix}$	Highest values |*SR*|	Coincident *MV* with calculated *MV*	Position in *SF*
1	42	11*	$\begin{pmatrix} 0.08117 & 0.0174 \\ 0.0174 & -0.00165 \end{pmatrix}$	49.19	None	20
		3*	$\begin{pmatrix} -0.06085 & 0.01592 \\ 0.01592 & -0.00166 \end{pmatrix}$	36.66	42-II	17
		2	$\begin{pmatrix} 0.08836 & 0.01694 \\ 0.01694 & -0.00266 \end{pmatrix}$	33.22	42-I	3
	43	11	$\begin{pmatrix} 0.0844 & 0.02039 \\ 0.02039 & 0.00485 \end{pmatrix}$	17.40	43-I	1
		3	$\begin{pmatrix} 0.06628 & 0.01601 \\ 0.01601 & 0.0039 \end{pmatrix}$	16.99	43-I	3
		12*	$\begin{pmatrix} -0.06199 & -0.02753 \\ -0.02753 & -0.00965 \end{pmatrix}$	6.42	43-I	22
	63	23*	$\begin{pmatrix} -0.1106 & -0.00142 \\ -0.00142 & 0.01677 \end{pmatrix}$	6.60	63-I	22
		18*	$\begin{pmatrix} 0.1014 & 0.01013 \\ 0.01013 & 0.0176 \end{pmatrix}$	5.76	63-II	18
		17	$\begin{pmatrix} 0.09701 & 0.0208 \\ 0.0208 & -0.03213 \end{pmatrix}$	3.02	63-II	6
2	76	22	$\begin{pmatrix} 0.05533 & -0.01444 \\ -0.01443 & -0.0001 \end{pmatrix}$	553.3	None	5
		17	$\begin{pmatrix} 0.077 & -0.01369 \\ -0.01369 & -0.00087 \end{pmatrix}$	88.51	76-I	3
		20*	$\begin{pmatrix} -0.044 & 0.05097 \\ 0.05097 & -0.00151 \end{pmatrix}$	29.14	None	17
	94	15	$\begin{pmatrix} 0.08542 & 0.00104 \\ 0.00104 & 0 \end{pmatrix}$	∞	94-I	3
		6	$\begin{pmatrix} 0.06532 & 0.00033 \\ 0.00033 & 0 \end{pmatrix}$	∞	94-I	5
		5*	$\begin{pmatrix} -0.07623 & -0.03618 \\ -0.03618 & 0.0004 \end{pmatrix}$	190.58	94-I	20
	96	22*	$\begin{pmatrix} 0.08413 & -0.02460 \\ -0.02460 & 0.0005 \end{pmatrix}$	168.26	None	23
		18	$\begin{pmatrix} 0.09087 & 0.00532845 \\ 0.00533 & -0.00081 \end{pmatrix}$	112.19	96-I	2
		23	$\begin{pmatrix} 0.073 & 0.00071 \\ 0.00071 & -0.0018 \end{pmatrix}$	40.56	None	4

* $\boldsymbol{\varepsilon_{xo}}$ negative.

In this case, we compared the 24 *MVs* plotted for each grain and the *MV* with the highest absolute value of strain ratio (|*SR*|).

The same analysis was also applied to the grains reported by Kaouache et al. [27]; the results are summarized in Table 7.

Table 7. Strain tensor analysis for the grains reported by Kaouache et al. [27] using the model of Cortés-Pérez [29].

Sample	Grain	Expected *MVs*	Strain tensor $\begin{pmatrix} \varepsilon_{x0} & \gamma_{xyo} \\ \gamma_{xy0} & \varepsilon_{yo} \end{pmatrix}$	Maximum values |*SR*|	Coincident *MV* with calculated *MV*	Position in *SF*
P1	A1	4	$\begin{pmatrix} 0.09755 & -0.04089 \\ -0.04164 & 0.01391 \end{pmatrix}$	7.01	A1-I	1
		10	$\begin{pmatrix} 0.08854 & -0.04095 \\ -0.04164 & 0.01595 \end{pmatrix}$	5.55	None	2
		9*	$\begin{pmatrix} -0.07021 & 0.06329 \\ 0.06452 & -0.02603 \end{pmatrix}$	2.70	None	22
	B1	21	$\begin{pmatrix} 0.07463 & -0.04801 \\ -0.04858 & 0.00060 \end{pmatrix}$	124.38	B1-III	3
		19*	$\begin{pmatrix} -0.07887 & 0.01508 \\ 0.01528 & -0.00072 \end{pmatrix}$	109.54	None	19
		24*	$\begin{pmatrix} -0.05748 & 0.01657 \\ 0.01684 & -0.00153 \end{pmatrix}$	37.57	None	17
	C1	20*	$\begin{pmatrix} -0.10456 & -0.03355 \\ -0.0344 & 0.00139 \end{pmatrix}$	75.22	C1-II	23
		21*	$\begin{pmatrix} -0.09305 & -0.03988 \\ -0.04062 & -0.00328 \end{pmatrix}$	28.37	C1-III	18
		19	$\begin{pmatrix} 0.07585 & 0.06567 \\ 0.06703 & 0.00465 \end{pmatrix}$	16.31	C1-II	8
P2	A2	4*	$\begin{pmatrix} -0.04876 & -0.0531 \\ -0.05455 & 0.00011 \end{pmatrix}$	443.27	A2-II	20
		5*	$\begin{pmatrix} -0.03405 & 0.08884 \\ 0.09024 & -0.00024 \end{pmatrix}$	141.86	A2-II	16
		23	$\begin{pmatrix} 0.08958 & -0.05145 \\ -0.05174 & 0.00237 \end{pmatrix}$	37.80	A2-II	2

* ε_{xo} negative.

Tables 6 and 7 provide a list of the strain tensors in the observation system according to the model of Cortés-Pérez [29] and the |*SR*| for each expected *MV* (only the first three cases satisfying these conditions were analyzed). In these tables, the positions of the three *MVs* with higher |*SR*| reflect the order of the *SF* from maximum to minimum. The *MVs* with a high |*SR*| are coincident for the majority of all studied grains. However, several cases or inconsistencies were observed in the comparison of Tables 2, 3, 4 and 5 with Tables 6 and 7, as described below.

a) In some cases, the ε_{x0} values are negative; however, this situation is not possible because deformation against the movement is implicated. In other words, these values indicate negative *SFs*. Therefore, these values for the *SR* criterion should be discarded in this analysis. For example, *MVs* 11 and 3 in grain 42 present the case mentioned above; the maximum |*SR*| in grain 42 is present in *MV* 2. For this reason, the *MV* with negative ε_{x0} will be discarded in the next subsections. Therefore, the next |*SR*| with a positive value of ε_{x0} will be considered the maximum |*SR*|. Despite the aforementioned information, possible negative values of ε_{x0} in *MVs* were found that coincided with the real *MV* formed. For example, the *MV* 23 in grain 63 is coincident with real *MV* 63-I.

b) If an *MV* has a higher |*SR*|, it may coincide instead of the *MV* with the higher *SF* (this result occurs for grains 42, 94, and 96 in our sample).

c) Despite there being an *MV* with the maximum |*SR*|, this does not imply that this *MV* will appear. For example, grain 76 indicated that *MV* 22 with a high |*SR*| did not coincide with the *MV* plotted.

d) For each real *MV* formed in a grain, two or more *MVs* that are coincident with this *MV* may exist. For example, in grain 43, *MVs* 11 and 3 presented a high |*SR*| and the same line in the observation system; however, only one of these *MVs* was formed (Figure 4a). It is difficult to select an *MV* when the *MVs* present very similar values.

e) For grains with two or three real *MVs* formed, it is not possible to know which *MVs* coincide with the principal or which will grow first, e.g., grains 42, 63, B1, C1 and A2.

f) Some grains present *MVs* with very similar value of *SF*; however, only one is coincident, e.g., grain 63 and its *MVs* 19 and 2.

g) Values of |*SR*| with infinite value are always coincident, e.g., *MVs* 15 and 6 of grain 94.

For both criteria, the *SF* and |*SR*| clearly presented some inconsistencies with the real *MVs* formed. Therefore, it was not possible to predict which *MV* would appear.

For these reasons, a new criterion involving a combination of both the *SF* and |*SR*| (or *SR* and $-\varepsilon_{x0}$) criteria was proposed in this research. This criterion involves the following considerations:

1) *MVs* with negative *SF* are discarded.

2) *MVs* with |*SR*| < 1 are discarded because this situation implies that $\in_{xo}$ is less than $\in_{yo}$; furthermore, this state of strain is not favored by the applied load direction (*RD*), as shown in Figure 7.

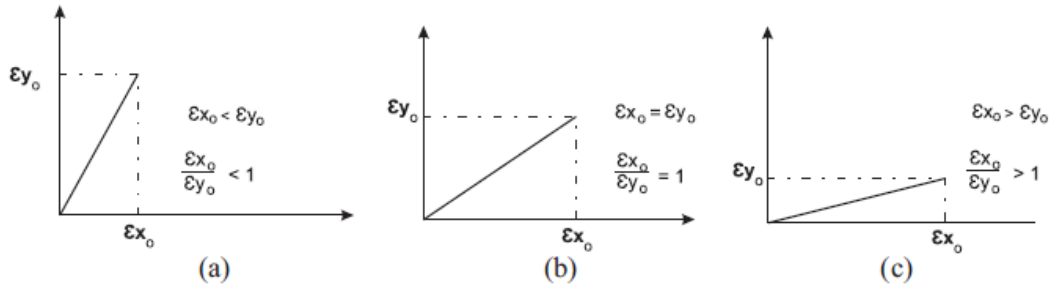

Figure 7. Cases presented for |*SR*|. a) Deformation near *TD*. b) Deformation of the middle of *TD* and *RD*. c) Deformation near *RD*.

3) A balance criterion (*BC*) based on the following equations should be used with the remaining *MVs*:

If $SF_P \leq SR_P$ $BC = (SF_P - SR_P) + O_v$ (16a)

and if $SR_P \leq SF_P$ $BC = (SR_P - SF_P) + O_v$ (16b)

where SF_P and SR_P are the positions of *SF* and *SR* respectively. O_v is an integer number with a maximum value of 10 that prioritizes the positions of *SF* and/or *SR* that were not discarded under considerations 1 and 2.

Table 8 presents the complete list of the |*SR*| and *SF* values for grain 42. Notice that |*SR*| does not depend on the shear amplitude. In this table, our proposed criteria were applied until consideration 2, and the coincident *MVs* (A) and the discarded *MVs* (C, D) were labeled with letters. The coincident *MVs* are presented in Table 2. The predicted *MVs* were then 2, 12, 4, and 10, as shown in Table 9.

Table 9 shows the *MVs* with status A and B (or only B) according to Table 8. In both cases, the same *MVs* are obtained for |*SR*| and *SF*; however, their order of appearance differs. For this reason, the third consideration must be included (this last consideration is not necessary if the *SR* and $-\varepsilon_{x0}$ are considered). We took into account both criteria (|*SR*| and *SF*); until now, these criteria have had the same importance, and their influence has been weakened

when their values are small. *MV* 2 has the same position (3^{rd}) for the |*SR*| and *SF*; therefore, this *MV* is the first *MV* with the greatest probability of appearing.

Table 8. Selected *MVs* using the |*SR*|-*SF* criterion for grain 42.

(A) Coincident *MV* according to Table 2 (B) *MV* with a high probability of appearing

(C) Discarded *MV* with negative *SF* (D) Discarded *MV* with |*SR*| < 1

Grain 42					
|*SR*|	*MV*	Status	*SF*	*MV*	Status
49.09	11	C	0.47	19	D
36.62	3	A, C	0.42	24	D
33.17	2	A, B	0.38	2	A, B
30.74	12	B	0.30	17	D
5.69	9	A, C	0.30	4	A, B
5.43	4	A, B	0.30	12	B
5.20	10	A, B	0.26	22	D
3.95	1	C	0.22	10	A, B
0.98	19	D	0.17	16	D
0.96	24	D	0.15	7	D
0.94	23	D	0.02	13	D
0.86	18	D	0.002	14	D
0.83	20	D	-0.009	5	C
0.83	21	D	-0.02	8	C
0.62	17	D	-0.08	15	C
0.57	22	D	-0.08	6	C
0.36	16	D	-0.26	3	C
0.34	7	D	-0.31	1	C
0.18	15	D	-0.33	18	C
0.17	6	D	-0.35	11	C
0.04	13	D	-0.38	9	A, C
0.04	8	D	-0.38	20	C
0.02	5	D	-0.39	23	C
0.003	14	D	-0.41	21	C

Table 9. *MVs* predicted using the |*SR*|-*SF* criterion for grain 42.

(A) Coincident *MV* according to Table 2 (B) *MV* with a high probability of appearing

Grain 42								
SR_P*	|*SR*|	*MV*	Status	SF_P**	*SF*	*MV*	Status	Order value (O_v)
3^{rd}	33.17	2	A, B	3^{rd}	0.38	2	A, B	10
4^{th}	30.74	12	B	4^{th}	-	-	-	9
5^{th}	-	-	-	5^{th}	0.30	4	A, B	8
6^{th}	5.43	4	A, B	6^{th}	0.30	12	A, B	7
7^{th}	5.20	10	A, B	7^{th}	-	-	-	6
8^{th}	-	-	-	8^{th}	0.22	10	A, B	5

*Strain ratio position. **Schmid factor position.

However, the aforementioned condition is not always present; for example, *MV* 12 occupies the 4th position according to the |*SR*| value but the 6th position with respect to *SF*. In this case, it is difficult to predict the order of *MV* formation. For this reason, a *BC* was introduced. This balancing criterion is used to propose an ordering of *MVs* by probability of appearance based on an assigned order value (O_v), which will depend on the largest values of the |*SR*| position (SR_P) and *SF* position (SF_P). This *BC* is summarized in equations 16a and 16b. Note that if $SF_P = SR_P$, both equations can be used interchangeably. For example, the ideal case occurs when an *MV* has the same position in |*SR*| and *SF* and their values are maximal. In *MV 2*, we obtained a *BC* value of 10 using equation 16a or 16b, $BC = ([3 - 3] + 10 = 10)$; this value indicates the best balance and corresponds to *MV* 2. *MV* 12 is in the fourth position according to the |*SR*| but the sixth position according to its *SF*; this condition has a *BC* value of 7 (in this case, equation 16b was used because $SR_P \leq SF_P$ $([4 - 6] + 9 = 7)$). Following the *BC* and their conditions, the order of growth was determined for *MVs* 4, 10 and 12 in grain 42, as shown in Table 10. The predicted *MVs* are shown in Figure 8.

Table 10. Possible order of growth of *MV*s predicted according to the *BC* between |*SR*| and *SF* for grain 42.

Grain 42	
MV	BC Value
2	10
12	7
4	6
10	5

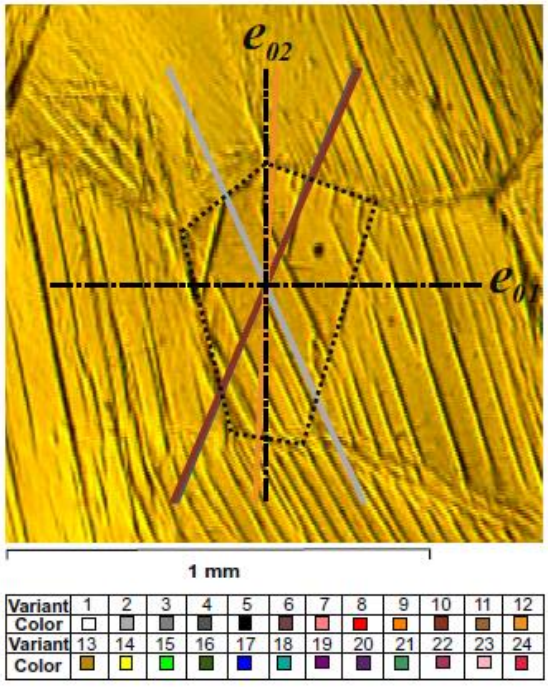

Figure 8. Predicted *MVs* for grain 42 of region 1.

Similarly, the |*SR*| and *SF* values for grain 96 are presented in Table 11.

When the methodology used for grain 42 was applied to grain 96, the predicted *MVs* were 18, 23, 20, and 21. *MV* 18 was the most balanced because this *MV* had high values of both *SF* and |*SR*|; this *MV* was the principal *MV* predicted, and it had a *BC* value of 10. The next *MVs*, 23 and 20, did not have a similar equilibrium relation and had *BC* values of 7 and 3, respectively. Finally, *MV* 21 had a similar position but less balance than the previous *MVs* ($[8-8]+2=2$). The predicted *MVs* are shown in Figure 9.

Table 11. Selected *MVs* using the |*SR*|-*SF* criterion for grain 96.

(A) Coincident *MV* according to Table 2 (B) *MV* with a high probability of appearing

(C) Discarded *MV* with negative *SF* (D) Discarded *MV* with |*SR*| < 1

Grain 96					
|*SR*|	*MV*	Status	*SF*	*MV*	Status
168	22	C	0.41	13	D
112.73	18	A, B	0.39	18	A, B
40.6	23	B	0.33	8	D
12.74	17	A, C	0.31	23	B
7.31	24	C	0.25	15	D
5.06	19	C	0.25	20	B
1.86	20	B	0.19	6	D
1.52	21	B	0.19	21	B
0.97	13	D	0.12	2	D
0.96	8	D	0.10	3	D
0.87	7	D	0.08	12	D
0.87	14	D	0.05	11	D
0.86	5	D	-0.03	4	C
0.80	16	D	-0.05	1	C
0.59	15	D	-0.05	10	C
0.52	6	D	-0.07	9	C
0.29	3	D	-0.23	19	C
0.27	2	D	-0.24	16	C
0.20	12	D	-0.30	17	A, C
0.15	11	D	-0.32	14	C
0.14	9	D	-0.32	24	C
0.13	10	D	-0.32	7	C
0.11	1	D	-0.36	22	C
0.08	4	D	-0.37	5	C

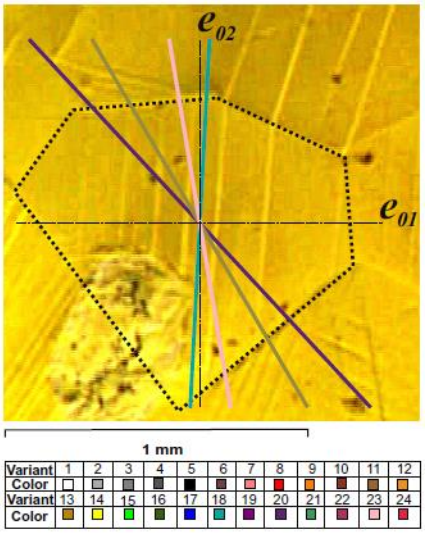

Figure 9. Predicted *MVs* for grain 96 of region 2.

Finally, the application of our criteria for grain A1 is presented in Table 12.

Table 12. Selected *MVs* using the |*SR*|-*SF* criterion for grain A1 of Kaouache et al. [27].

(A) Coincident *MV* according to Table 4 (B) *MV* with a high probability of appearing

(C) Discarded *MV* with negative *SF* (D) Discarded *MV* with |*SR*| < 1

Grain A1					
|*SR*|	*MV*	Status	*SF*	*MV*	Status
7.01	4	A, B	0.42	4	A, B
5.55	10	B	0.38	10	B
2.70	9	C	0.26	6	B
2.11	23	C	0.24	24	B
2.01	11	A, C	0.23	15	B
2.01	3	A, C	0.21	2	D
1.74	1	C	0.18	12	A, D
1.42	18	C	0.17	22	D
1.23	6	B	0.14	19	B
1.17	15	B	0.07	17	D
1.05	19	B	0.05	8	D
1.04	24	B	0.03	13	D
0.98	20	D	-0.06	7	C
0.96	21	D	-0.10	21	C
0.79	22	D	-0.10	16	C
0.78	2	D	-0.15	5	C
0.69	17	D	-0.16	23	C
0.63	12	A, D	-0.16	14	C
0.53	5	D	-0.21	20	C
0.49	14	D	-0.25	1	C
0.32	16	D	-0.25	18	C
0.19	7	D	-0.30	9	C
0.12	8	D	-0.32	3	A, C
0.08	13	D	-0.33	11	A, C

In this case, more *MVs* satisfied the proposed criteria, with the following order of possible growth: 4, 10, 6, 15, 19, and 24. This order is based on the *BC* values. *MVs* 4 and 10 exhibited higher *BC* values of 10 and 9, respectively. The *BC* of the remaining *MVs* was small. For example, the next *MVs*, 6 and 15, had *BC* values of 2 and 1, and the last *MVs*, 19 and 24, actually had zero or negative values under our criterion. The 6 predicted *MVs* for this case are presented in Figure 10.

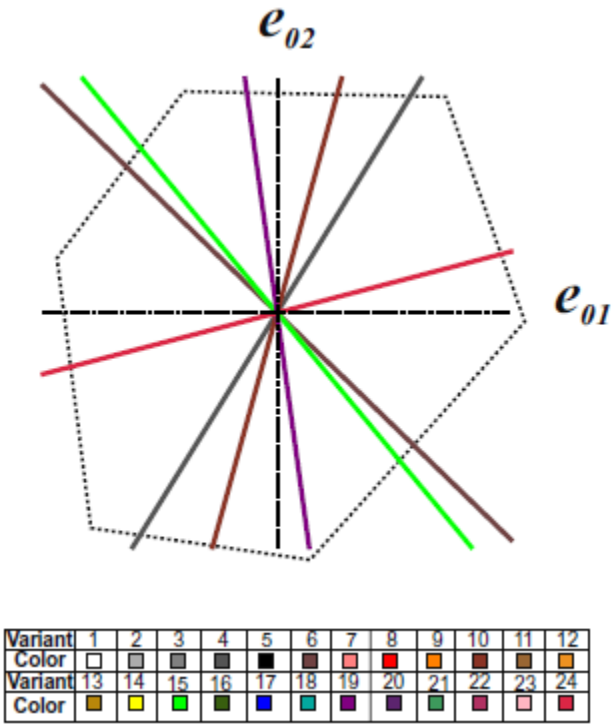

Figure 10. Predicted *MVs* for grain A1 of sample P1 from Kaouache et al. [27].

Table 13 presents the predicted *MVs* for all the grains studied here.

Table 13. Summary of the results applying the *BC* for grains of our sample and those of Kaouache et al. [27].

Grain	Expected *MVs* with *BC*	Number of formed *MVs* per grain	Coincident *MVs*
42	2, 12, 4, 10	I	2
		II	4, 10
43	11, 3	I	11, 3
63	17, 24, 19, 22, 12, 2, 4, 10	I	24
		II	19, 10
		III	17, 24
76	22, 17, 19, 24, 2, 12	I	17
94	15, 6, 13, 8	I	15, 6
96	18, 23, 20, 21	I	18
A1	4, 10, 6, 15, 19, 24	I	4
B1	21, 20, 23, 18, 6, 15	I	6
		II	15
		III	21
C1	24, 19, 22, 17, 4, 2, 10, 12	I	24, 17, 10
		II	19
		III	22
A2	23, 11, 18, 3, 15, 20	I	18
		II	23
		III	3

All maximum values for *BC* are shown in the second column, whereas the *MVs* that are coincident with the *BC* according to the *MVs* listed in Tables 2 and 4 are shown in the last columns. For example, the expected *MVs* in grain 42 are 2, 12, 4, and 10; however, only *MVs* 2, 4 and 10 have lines that are coincident with the *MVs* formed. Therefore, these *MVs* are predicted in grain 42. Similarly, the *MVs* predicted in the other grains are selected using the methodology described above. Close agreement is observed between our proposed criteria and the actual *MVs* formed in all the grains studied because the expected *MV* always appeared.

The proposed *BC* is in agreement with the experimental results but exhibits some inconsistencies. a) For example, in grain 42, *MVs* 4 and 10 are coincident with a real formed *MV*. The cases for grains 43, 94, 96, and C1 are similar. b) *MVs* were predicted but not observed at that particular state of stress when the metallographic images were captured. For example, in the case of grain A1, *MV* 10 was formed according to Kaouache et al. [28]; however, *MV* 10 was inhibited under the high-stress condition.

To improve the proposed criterion, we included the in-plane *STDs* as a discrimination tool, which allows us to predict the stress-induced *MV* in a polycrystalline *SMA* when combined with our *BC* developed above. Thus, we calculated the transformation diagrams for all the studied grains using the procedure presented by Buchheit et al. and Comstock et al. [14, 15]. Figure 11 presents the *STDs* for region 1 and their location in the inverse pole diagram. The *STD* diagrams are valid for an in-plane state of stress in single crystals.

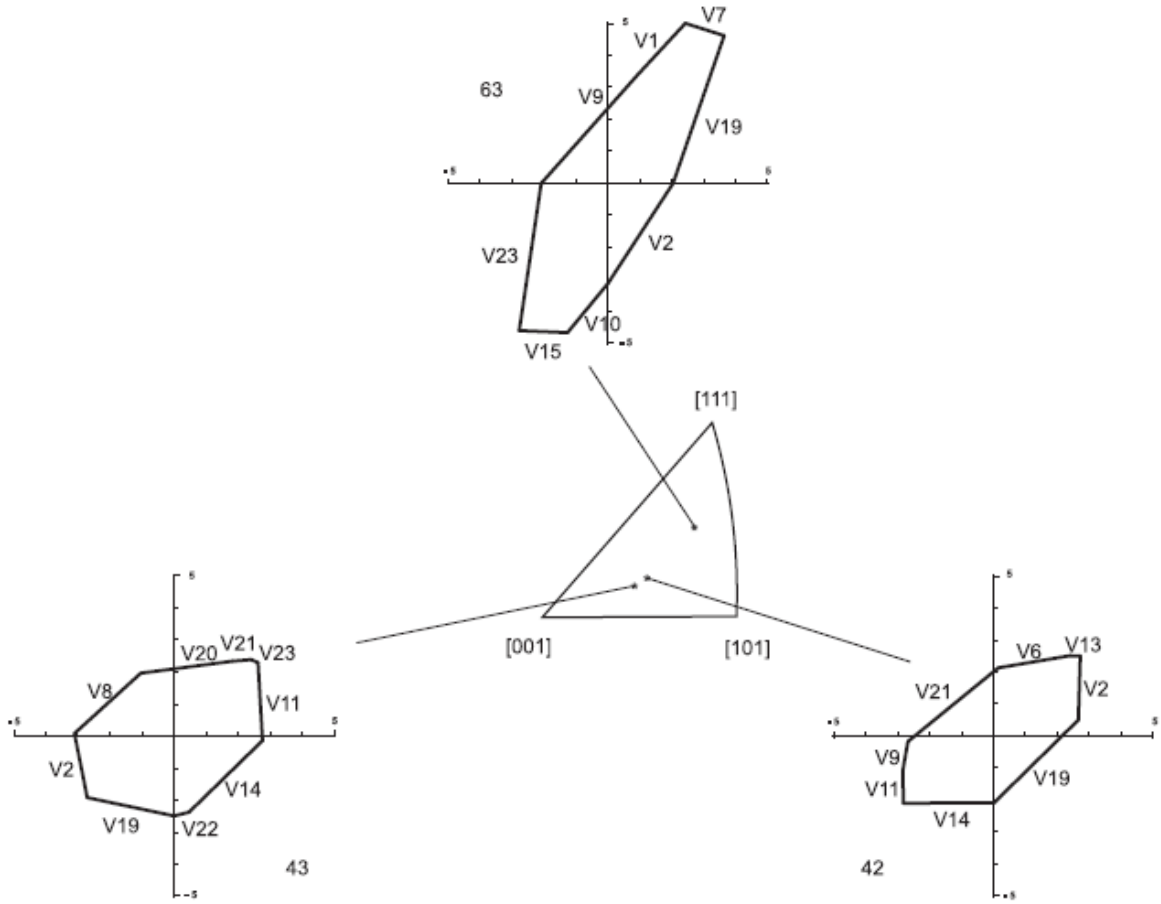

Figure 11. *STDs* for region 1 involving grains 42, 43, and 63; these diagrams present the predicted *MVs* as a function of the crystal orientation and state of stress.

The *STD* has four quadrants (according to a Cartesian system) with different states of stress: the first quadrant corresponds to tension-tension (*T*-*T*), the second quadrant to compression-tension (*C*-*T*), the third quadrant to compression-compression (*C*-*C*) and the fourth quadrant to tension-compression (T-*C*). For example, *MVs* 1, 7, and 19 will appear in grain 63 if the state of stress is *T*-*T*, as shown in Figure 11. However, these diagrams should be modified for polycrystals because of the *GI* effect. Figure 12 presents the transformation diagram for the grains of our sample, and Figure 13 presents the transformation diagrams for the grains studied by Kaouache et al. [27]. Figures 12 and 13 consider the coincident

MVs listed in Tables 2 and 4, respectively, whereas the *MVs* expected with the *BC* are shown in Table 13.

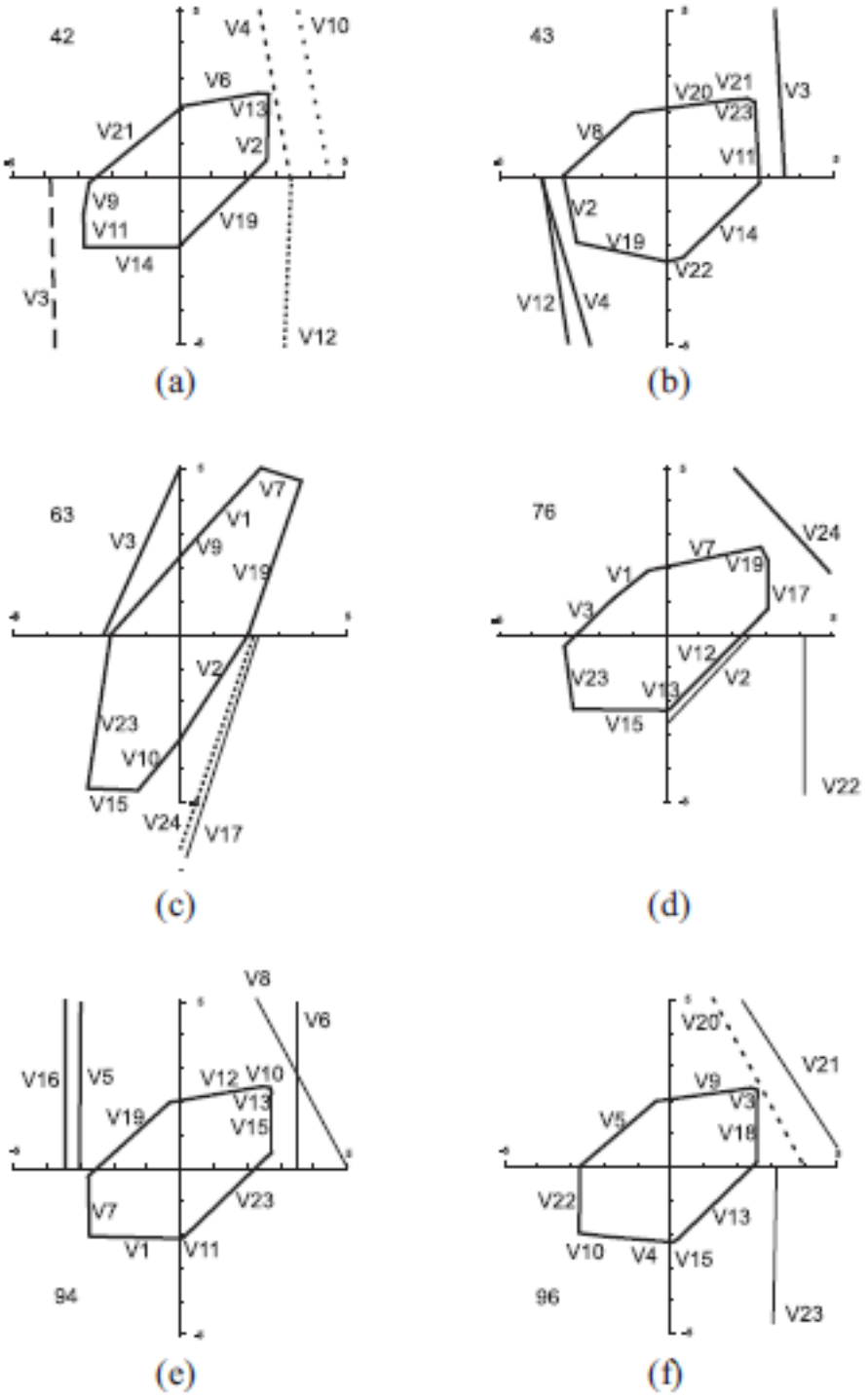

Figure 12. Calculated *STDs* for the grains 42, 43, 63, 76, 94, and 96 in the Cu-Al-Be system.

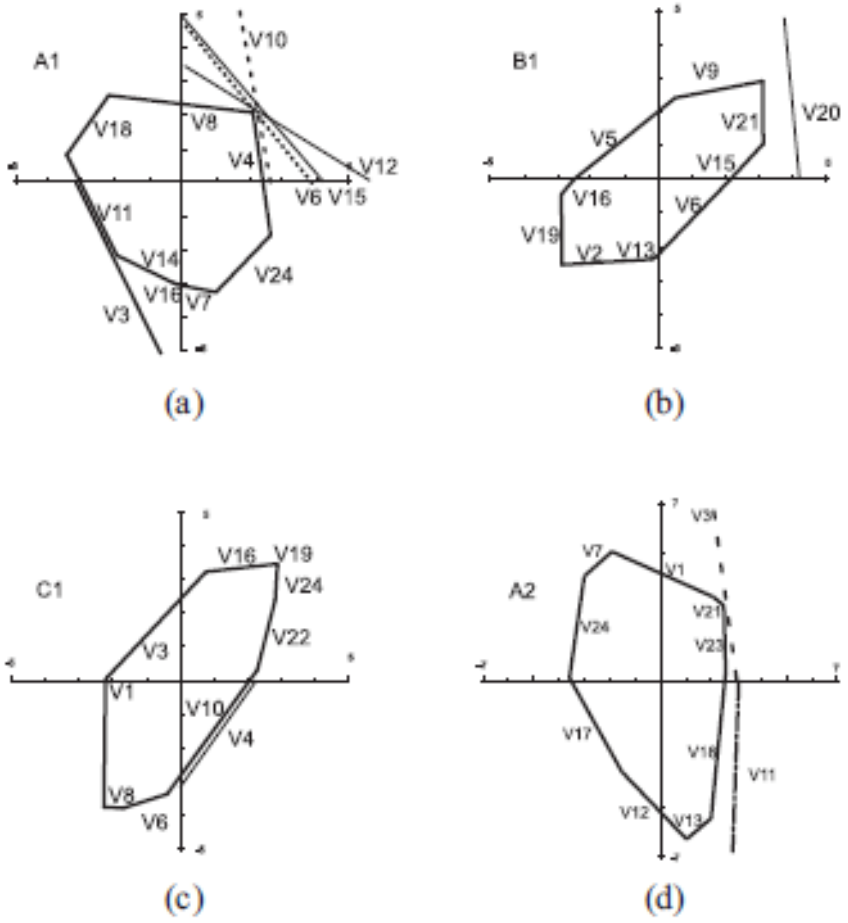

Figure 13. Calculated *STDs* for the grains A1, B1, C1, and A2 previously studied by Kaouache et al. [27].

In all grains, the *MVs* in the second and third quadrant are discarded because their states of stress differ from simple tension (*C*-*C* and *C*-*T*). Figure 12a presents the *STD* for grain 42. In this case, the *MVs* discarded in quadrants two and three are 9, 11, 14, and 21. The case of *MV* 3 is shown because this *MV* appeared in Table 2. In contrast, the *MVs* located in quadrants one and four have a high probability of appearing. In fact, if the grain boundary does not exist, the uniquely formed *MV* in tension will be *MV* 19; this *MV* corresponds to the maximum *SF*. However, this *MV* is discarded by the *BC*; therefore, according to the

proposed criterion, *MV* 2 is expected and is in agreement with the *STD*. The next predicted *MVs* with the *BC* criterion are *MVs* 4, 12 and 10; the transformation diagram clearly illustrates that *MV* 4 has the highest probability of appearing because less energy is needed for its formation. In the case of *MVs* 6 and 13, the state of stress is high in the *TD*, and these *MVs* are discarded as well. Finally, *MVs* 2 and 4 are the predicted *MVs* for the combination of the |*SR*|-*SF* criterion and the transformation diagram. In the case of grain A1, the discarded *MVs* in quadrants two and three are 8, 18, 11, 14, 16, 7 and 3. The expected *MVs* for *BC* are 4, 10, 6, 15, 19 and 4; the *MV* predicted in this case is clearly *MV* 4. This *MV* has the maximum *SF* and is uniquely formed according to Kaouache et al. [27]. The mechanism is shown in *BC*; this *MV* has the highest *BC* values, and the other *MVs* are less likely to appear. However, *MV* 10 has a good *BC* relation; in fact, this *MV* was formed at low deformation, in agreement with Kaouache [28].

Finally, this methodology was applied to all the studied grains, and the results were consistent with the proposed criterion. The final criterion is the combination of *BC* and *STD*, and the *SIMT* need not be observed in situ. Importantly, using our methodology and the Cortés-Pérez model [29], the mechanical behavior of a polycrystalline Cu-Al-Be *SMA* may be estimated if the crystalline orientation is known. Furthermore, our methodology can be applied to study the yield in conventional polycrystalline materials because the mechanism of martensitic transformation is similar to the slip plane, which is well known and relevant to explaining yield. A summary of the predictions for all the studied grains is provided in Table 14.

Table 14. Summary of the results of the *MVs* predicted with the *BC-STD* criterion.

Grain	Number of *MVs* formed	Variants predicted with *BC-STD*
42	I	2
	II	4
43	I	11
63	I	24
	II	19
	III	17
76	I	17
94	I	15
96	I	18
A1	I	4
B1	I	6
	II	15
	III	21
C1	I	10
	II	19
	III	22
A2	I	18
	II	23
	III	3

4. Conclusions

According to the literature, the nature of the *SIMT* can be studied using the *SF* criterion; however, in our research, some inconsistencies have been observed for specific grains. Our results demonstrate that grain boundary interaction modifies the state of stress that favors or inhibits the growth of specific *MVs*; this modification explains why the third or second *MV* with a high *SF* value grows instead of the *MV* with maximum *SF*. To better understand the nature of the *SIMT*, the *SR* was used. However, the use of the *SF* and |*SR*| criteria to predict the formation of *MVs* resulted in several inconsistencies. Furthermore, the *BC-STD* criterion, which predicts which *MVs* have a high probability of appearing and the possible order of formation of *MVs*, was developed. To apply our criterion, the following parameters must be considered: the crystallographic orientation, transformation system, critical

temperatures of transformation, grain geometry, magnitude of shear, test temperature, and magnitude of the applied normal stress during the uniaxial tensile test. Although the *BC-STD* criterion does not consider the interaction between martensitic-martensitic variants or changes in the stress distribution associated with evolution/reorientation of *MVs*, the *BC-STD* criterion shows good agreement with the experiment results. In addition, it demonstrates the strong influence of crystallographic orientation in the *MVs* formed during the *SIMT*.

Acknowledgments

The authors wish to thank the Coordinación de estudios de posgrado (CEP)-UNAM, PAPIIT project number TI 02414 and Instituto de Tecnología de Materiales-UPV for financial support. The authors are grateful to the Electron Microscopy Service of the UPV and especially to Manuel Josep Planes Insausti and José Luis Moya López. The authors are grateful to Martin Estrada Arcos, Alberto Higuera García, and Antonio González Montaño for their technical support.

References

[1] K.N. Melton, General applications of *SMA*'s and smart materials, in: K. Otsuka, C.M. Wayman (Eds.), Shape memory materials, Cambridge University Press, Cambridge, 1998, pp. 220-239.

[2] P.K. Kumar, D.C. Lagoudas, Introduction to shape memory alloys, in: D.C. Lagoudas (Ed.), Shape memory alloys. Modeling and engineering applications, Springer, New York, 2008, pp. 1-43.

[3] H. Tobushi, K. Date, K. Miyamoto, Characteristics and development of shape-memory alloys heat engine, J. Solid. Mech. Mater. Eng. 4 (2010) 1094-1102.

[4] K. Kaneko, K. Enomoto, Development of reciprocating heat engine using shape memory alloys, J. Environ. Eng. 6 (2011) 131-139.

[5] J.J. Zhu, N.G. Liang, K.M. Liew, W.M. Huang, Energy conversion in shape memory alloy heat engine Part I: Theory, J. Intell. Mater. Syst. Struct. 12 (2001) 127-132.

[6] J.J. Zhu, N.G. Liang, W.M. Huang, K.M. Liew, Energy conversion in shape memory alloy heat engine Part II: Simulation, J. Intell. Mater. Syst. Struct. 12 (2001) 133-140.

[7] K. Otsuka, C.M. Wayman, Mechanism of shape memory effect and superelasticity, in: K. Otsuka, C.M. Wayman, (Eds.), Shape Memory Materials, Cambridge University Press, Cambridge, 1998, pp. 27-48.

[8] V. Novák, P. Š ittner, N. Zárubová, Anisotropy of transformation characteristics of Cu-base shape memory alloys, Mater. Sci. Eng. A.234 236 (1997) 414-417.

[9] V. Novák, P. Š ittner, D. Vokoun, N. Zárubová, On the anisotropy of martensitic transformations in Cu-based alloys, Mater. Sci. Eng. A.273 275 (1999) 280-285.

[10] K. Otsuka, X. Ren, Physical metallurgy of Ti–Ni-based shape memory alloys, Prog. Mater. Sci. 50 (2005) 511-678.

[11] K. Taillard , S. Arbab Chirani, S. Calloch, C. Lexcellent, Equivalent transformation strain and its relation with martensite volume fraction for isotropic and anisotropic shape memory alloys, Mech. Mater. 40 (2008) 151-170.

[12] E. Patoor, D.C. Lagoudas, P.B. Entchev, L.C.Brinson, X.Gao, Shape memory alloys, Part I: General properties and modeling of single crystals, Mech. Mater. 38 (2006) 391-429.

[13] X. Gao, M. Huang, L.C. Brinson, A multivariant micromechanical model for SMAs Part 1. Crystallographic issues for single crystal model, Int. J. Plast. 16 (2000) 1345-1369.

[14] T.E. Buchheit, J.A. Wert, Modeling the effects of stress state and crystal orientation on the stress-induced transformation of Ni-Ti single crytals, Metall. Mater. Trans. A25 (1994) 2383-2389.

[15] R.J. Comstock, T.E. Buchheit, M. Somerday, J.A. Wert, Modeling the transformation stress of constrained shape memory alloy single crystals, Acta. Mater. 44 (1996) 3505-3514.

[16] B.C. Goo, C. Lexcellent, Micromechanics-based modeling of two-way memory effect of a single crystalline shape-memory alloy, Acta. Mater. 45 (1997) 727-737.

[17] D.C. Lagoudas, P.B. Entchev, P. Popov, E. Patoor, L.C. Brinson, X. Gao, Shape memory alloys, Part II: Modeling of polycrystals, Mech. Mater. 38 (2006) 430-462.

[18] Z.K. Lu, G.J. Weng, A self-consistent model for the stress-strain behavior of shape-memory alloy polycrystals, Acta. Mater. 46 (1998) 5423-5433.

[19] M. Panico, L.C. Brinson, A three-dimensional phenomenological model for martensite reorientation in shape memory alloys, J. Mech. Phys. Solids. 55 (2007) 2491-2511.

[20] P. Š ittner, V. Novák, Experiment feedbacks in micromechanics modeling of thermomechanical behaviors of SMA polycrystals, Scr. Mater. 51 (2004) 321-326.

[21] S. Montecinos, A. Cuniberti, A. Sepúlveda, Grain size and pseudoelastic behaviour of a Cu–Al–Be alloy, Mater. Charact. 59 (2008) 117-123.

[22] S. Berveiller, B. Malard, J. Wright, E. Patoor, G. Geandier, In situ synchrotron analysis of lattice rotations in individual grains during stress-induced martensitic transformations in a polycrystalline CuAlBe shape memory alloy, Acta. Mater. 59 (2011) 3636-3645.

[23] N. Siredey, E. Patoor. M. Berveiller, A. Eberhardt, Constitutive equations for polycrystalline thermoelastic shape memory alloys. Part I. Intragranular interactions and behavior of the grain, Int. J. Solids. Struct. 36 (1999) 4289-4315.

[24] F.M. Sánchez-Arévalo, G. Pulos, Use of digital image correlation to determine the mechanical behavior of materials, Mater. Caracter. 59 (2008) 1572-1579.

[25] R.J. Martínez-Fuentes, F.M. Sánchez-Arévalo, F.N. García-Castillo, G.A. Lara-Rodríguez, J. Cortés-Pérez, A. Reyes-Solís, Micromechanical Behavior of CuAlBe Shape Memory Alloy Undergoing 3-Point Bending Analyzed by Digital Image Correlation, in: Francisco Manuel Braz Fernandez (Ed.), Shape Memory Alloys - Processing, Characterization and Applications, InTech, Rijeka, 2013, pp. 197-212.

[26] N. Bourgeois, F. Meraghni, T.B. Zineb, Measurement of local strain heterogeneities in superelastic shape memory alloys by digital image correlation, Phys. Procedia. 10 (2010) 4-10.

[27] B. Kaouache, K. Inal, S. Berveiller, A. Eberhardt, E. Patoor, Martensitic transformation criteria in Cu–Al–Be shape memory alloy—In situ analysis, Mater. Sci. Eng. A. 438-440 (2006) 773-778.

[28] B. Kaouache, Doctorate Thesis, ENSAM, CER de Metz, 2006.

[29] J. Cortés, PhD. Thesis, Facultad de Ingeniería UNAM, Distrito Federal, 2007.

[30] S. Belkahla, PhD. Thesis, INSA Lyon, 1990.

[31] H. Flores. PhD. Thesis, Inst. Nat. Sc. Appl., Lyon, 1993.

[32] A. Tidu, A. Eberhardt, B. Bolle, F. Moreau, J.-J. Heizmann, Orthorhombic lattice deformation of CuAlBe shape-memory single crystals under cyclic strain, J. Appl. Cryst. 34 (2001) 722-729.

[33] A. Hautcoeur, A. Eberhard, E. Patoor, Berveiller. Termomechanical Behavior of Monocristalline Cu-Al-Be Shape Memory Alloys and Determination of the Metaestable Phase diagram. J. Phys. 05 (1995) 459-464.

[34] S. Kajiwara, Theoretical analysis of the crystallography of the martensitic transformation of BBC to 9R close-packed structure, Trans. Jpn. Inst. Met. 17 (1976) 435-446.

[35] J. Cortés-Pérez, J. G. González, J. Carrera, H. Flores. Mathematical analysis of experimental results in polycrystalline shape memory samples subject to a simple uniaxial tension test, in: P. Šittner, L. Heller and V. Paidar, Paidar (Eds.), ESOMAT 2009. The 8th European Symposium on Martensitic Transformations, Sciences, 2009, pp. 1-6.